Fabrication and Characterization of Advanced Triple-junction Amorphous Silicon Based Solar Cells

PHASE II – Quarter 3

Quarterly Technical Progress Report

September 1, 2006 to November 30, 2006

NREL Subcontract No. ZXL-5-44205-06

Subcontractor: The University of Toledo

Principal Investigator: Xunming Deng
(419) 530-4782; dengx@physics.utoledo.edu

Co-Principal Investigator: Robert W. Collins
(419) 530-2195; rcollins@physics.utoledo.edu

Department of Physics and Astronomy
University of Toledo, Toledo, OH 43606

Contract technical monitor: Dr. Bolko von Roedern

Table of Contents

Section 1

Executive Summary

This quarterly technical progress report covers the highlights of the research activities and results on the project of "The Fabrication and Characterization of High-efficiency Triple-junction a-Si Based Solar Cells" at the University of Toledo for the Period of September 1, 2006 to November 30, 2006, under NREL TFPPP subcontract number ZXL-5-44205-06.

Following this Executive Summary are the sections performed during this quarter related to the tasks under this subcontract. The major technical progresses of these sections are summarized as follows:

Section 2: Deposition Phase Diagram and Correlation with the Performance of a-Si:H Thin Film Solar Cells

A phase diagram has been developed to describe vhf plasma-enhanced chemical vapor deposition (PECVD) of hydrogenated silicon (Si:H) on a standard n-type a-Si:H layer, which is in turn deposited on crystalline Si held at a nominal temperature of 200°C. This Si:H is used as the topmost i-layer of a triple junction a-Si:H-based solar cell. In the deposition process, identical n/i cell structures were co-deposited on textured Ag/ZnO back-reflectors in order to provide correlations between the phase diagram and overall performance of solar cells completed through deposition of the p-layer and top contact. Studies of cell performance have shown that maximal open-circuit voltage and cell efficiency are obtained for an a-Si:H single junction cell when its i-layer is prepared at maximal hydrogen dilution -- i.e., just before crossing the a $\rightarrow$ (a + μc) phase boundary at the desired i-layer thickness. The phase diagram provides insights into how the efficiency for this top cell design can be improved with multistep processing.

Section 3: Origin of optical losses in Ag/ZnO back-reflectors for thin film Si photovoltaics

Real time SE has been applied to investigate the optical properties of Ag/ZnO interfaces in back-reflectors in the configuration used for n-i-p thin film Si solar cells. In particular, the effects of starting Ag surface roughness (d_s ~ 6 – 105 Å) on the nature of this interface have been explored. Even for the smoothest starting Ag surfaces (6 Å surface roughness thickness), a plasmon absorption band is detected in the optical properties of the observed ~ 40 Å thick interface layer. The characteristics of this band show a correlation with the starting Ag roughness layer, including a red shift in the plasmon peak energy with increasing d_s. We have corroborated the findings of real time SE using ex situ reflectance measurements, finding significant absorption losses in the visible range due to interference-enhanced plasmon absorption. For the specular Ag/ZnO studied here, these losses do not extend sufficiently far into the infrared to affect cell performance for ZnO deposited on relatively smooth Ag surfaces. When the underlying Ag surface roughness is thick enough (d_s ~ 100 Å) to significantly influence the nature of the interface dielectric function, optical losses due to the interface layer thickness and interference-enhanced plasmon absorption red-shift into the 1.2-1.5 eV range, where they are expected to strongly impact back-reflector performance in solar cells. Future efforts will be devoted to real time SE studies of Ag/ZnO further into the macroscopic roughness regime and to methods for mitigating the absorption losses in this regime.

Section 2

Deposition Phase Diagram and Correlation with the Performance of a-Si:H Thin Film Solar Cells

J. A. Stoke, Xinmin Cao, N. J. Podraza, Xunming Deng, and R. W. Collins

Department of Physics and Astronomy, University of Toledo, Toledo, OH 43606, USA

Overview

A phase diagram has been developed to describe vhf plasma-enhanced chemical vapor deposition (PECVD) of hydrogenated silicon (Si:H) on a standard n-type a-Si:H layer, which is in turn deposited on crystalline Si held at a nominal temperature of 200°C. This Si:H is used as the topmost i-layer of a triple junction a-Si:H-based solar cell. In the deposition process, identical n/i cell structures were co-deposited on textured Ag/ZnO back-reflectors in order to provide correlations between the phase diagram and overall performance of solar cells completed through deposition of the p-layer and top contact. Studies of cell performance have shown that maximal open-circuit voltage and cell efficiency are obtained for an a-Si:H single junction cell when its i-layer is prepared at maximal hydrogen dilution -- i.e., just before crossing the a → (a + μc) phase boundary at the desired i-layer thickness. The phase diagram provides insights into how the efficiency for this top cell design can be improved with multistep processing.

1. Introduction

State-of-the-art solar cells based on amorphous silicon (a-Si:H) prepared by plasma-enhanced chemical vapor deposition (PECVD) employ a triple-junction design [1,2]. Optimization of the a-Si:H i-layer component of the top cell has been widely successful by applying the concept of maximal H_2 dilution [3]. Potential benefits of H_2 dilution in general include enhanced precursor surface diffusion in the PECVD process, as well as sub-surface strained bond relaxation [4]. The resulting "protocrystalline" nature of the i-layer leads to the highest device performance and stability. In previous studies under such PECVD protocrystalline conditions, Si:H depositions on smooth, oxidized c-Si substrates exhibit the largest and most rapid smoothening during coalescence, the smoothest stable surface, as well as the largest thickness at which a roughening onset occurs in the amorphous growth regime [5]. In addition, studies of the dielectric function of the protocrystalline Si:H reveal the smallest broadening parameter yet observed for a-Si:H, indicating the highest short-range ordering. Because Si:H depositions performed on a-Si:H substrates (undiluted, R=0) lead to a structure of sufficient similarity to that used in solar cell deposition, a close correlation can be established between the measured phase evolution and the cell performance. In fact, proper interpretation of these phase diagrams has led to the optimization of one-step and two-step single junction p-i-n a-Si:H based solar cells [6].

Utilizing these same concepts, a deposition phase diagram has been developed for Si:H i-layers deposited on standard a-Si:H n-layers in order to establish similar optimization principles for the top junction of high-efficiency triple junction n-i-p solar cells. Crystal silicon (c-Si)

wafers, serving as the substrates for the standard n-layers, ensure a specular surface to aid in characterization of this system (PECVD a-Si:H from S_2H_6) for the first time by real time spectroscopic ellipsometry (RTSE). In order to achieve the desired deposition phase diagram from ellipsometry and correlate it with solar cell performance, additional samples were co-deposited on textured Ag/ZnO/(n-type a-Si:H) back-reflectors in the device configuration simultaneously with the specular c-Si/(native-oxide)/(n-type a-Si:H) substrates.

2. Experimental Details

The Si:H films for phase diagram development were deposited on c-Si/(native-oxide)/(n-type a-Si:H) substrate structures using multichamber vhf (70 MHz) PECVD for measurement in real time using a rotating-compensator multichannel ellipsometer [7], and the devices for performance characterization were deposited simultaneously on textured Ag/ZnO back-reflectors coated first with an n-layer. For all depositions performed versus the phase diagram variable $R = [H_2]/[Si_2H_6]$, all other parameters were selected as those used for the previously-optimized top i-layer of a triple junction device, including a low substrate temperature, nominally 200°C, a plasma power of 8 W, a low source gas $[Si_2H_6]$ partial pressure, $p < 0.004$ Torr, and a low total gas pressure, $p \sim 0.2$ Torr.

3. Results

Figure 1 shows two temperature calibrations that provide the true surface temperature of the crystalline silicon substrate from the nominal temperature under two conditions: vacuum and deposition pressure (0.2 Torr H_2). Such calibration is important because the thermocouple used for temperature measurement and control cannot be mounted close enough to the substrate surface to ensure an absolute measurement. These calibrations were obtained from the shifts relative to room temperature in the measured E_1 (~ 3.3 eV) and E_2 (~ 4.2 eV) peak energies, deduced from derivatives of the dielectric functions of the crystalline silicon substrate, in comparison with the known relationships [8] between the peak energies and true temperature.

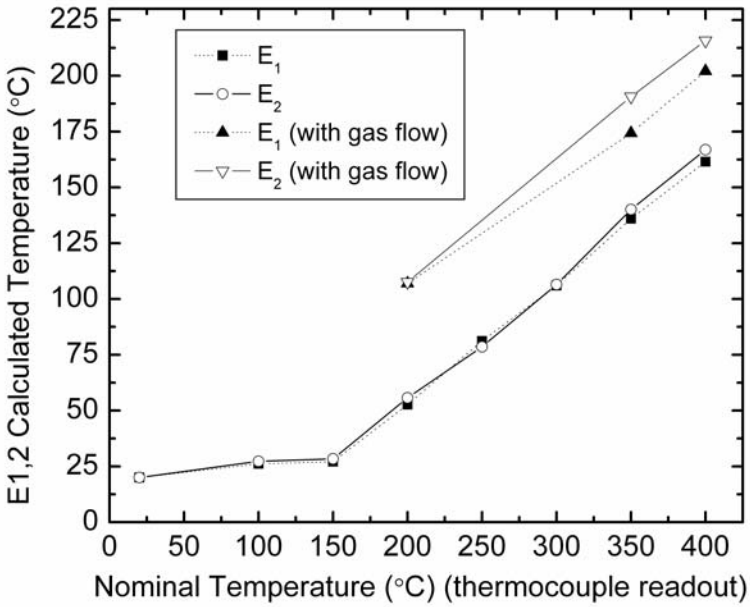

Fig. 1: Temperature calibrations for silicon substrates performed under vacuum and at 0.2 Torr H_2 pressure. To obtain these results the derivatives of the crystalline Si dielectric function were fit assuming two critical point parabolic band resonances to extract the resonance energies E_1 and E_2. A comparison of the energy shifts relative to known room temperature with a literature relationship [8] yields the calculated or true temperatures plotted on the ordinate.

Figure 2 depicts the dielectric function of the a-Si:H n-layer deposited on previously-measured native-oxide-covered c-Si. In fact, the c-Si substrate is measured by spectroscopic ellipsometry in-situ in the i-layer chamber of the system (before transfer to the n-layer chamber) in order to extract the oxide thickness and c-Si dielectric function at the deposition temperature. Then, the c-Si substrate is moved through a load lock to the n-layer chamber where an ~100 Å thick n-type a-Si:H layer is deposited. After n-layer deposition, the substrate is moved back to the i-layer chamber and measured by spectroscopic ellipsometry in order to extract the dielectric functions of the n-type material (as shown in Fig. 2) through an artifact minimization procedure [9]. This procedure models the n-layer as a dense bulk layer and an overlying surface roughness layer, the latter represented by a 0.50 (void) / 0.50 (n-type a-Si:H) volume fraction mixture with optical properties determined by the Bruggeman effective medium approximation [10]. By varying the bulk layer thickness (d_b) and surface roughness layer thickness (d_s) systematically in order to eliminate substrate-induced artifacts, an accurate dielectric function is obtained.

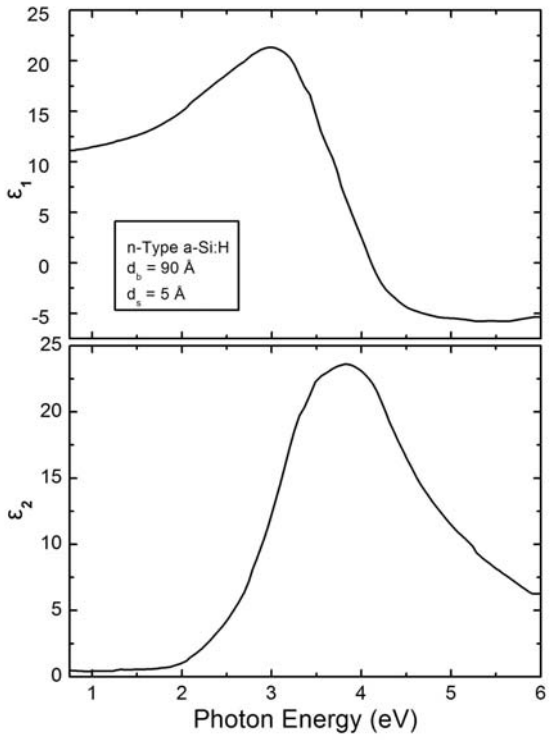

Fig. 2: Dielectric function of n-type a-Si:H determined by artifact minimization at a nominal temperature of 200°C. The bulk and surface roughness thicknesses are d_b = 90 Å and d_s = 5 Å, respectively. These dielectric functions are necessary in order to fully characterize the c-Si / (native-oxide) / (n-type a-Si:H) substrate which is the starting point for the i-layer depositions that establish the phase diagram.

Figure 3 shows the optical band gaps of the Si:H i-layer samples, in each case after deposited thicknesses of 150-250 Å, plotted versus the H_2-dilution flow ratio R. The results shown as the points and lower lines were obtained from real time spectroscopic ellipsometry (SE) data collected at the calibrated deposition temperature of 107°C (nominal 200°C) and deduced either from extrapolations of $\varepsilon_2^{1/2}$ versus E (solid symbols) or from complete fits using a parameterized Cody-gap-modified Lorentz oscillator [11,12] (open symbols). Both approaches are based on the assumptions of parabolic bands and a constant dipole matrix element. Films prepared over the range in R of 60 - 150 exhibit gaps within the range of 1.64 - 1.80 eV. Shown in Fig. 3 as the upper broken line is the result of two band gap adjustments: (i) an increase of

~0.04 eV as an adjustment from the true deposition temperature to room temperature [$\Delta T = (107 - 20)^{o}C = 87°C$ with a temperature coefficient of 4.5×10^{-4} eV/°C]; and (ii) another increase of ~ 0.04 eV attributed to the differences in optical gap extrapolation methodology, a more conventional approach being the assumption of a constant momentum matrix element due to Tauc [13]. Thus, the estimated room temperature Tauc gaps [extrapolations of $(\varepsilon_2 E^2)^{1/2}$ versus E, assuming parabolic bands and a constant momentum matrix element] shown as the upper broken line in Fig. 3 range from 1.72 eV for R=60 to 1.88 eV for R=150. These are the Tauc gaps one would expect to measure by transmission spectroscopy on thick films, when each gap is obtained by extrapolating data over photon energies just above the band gap.

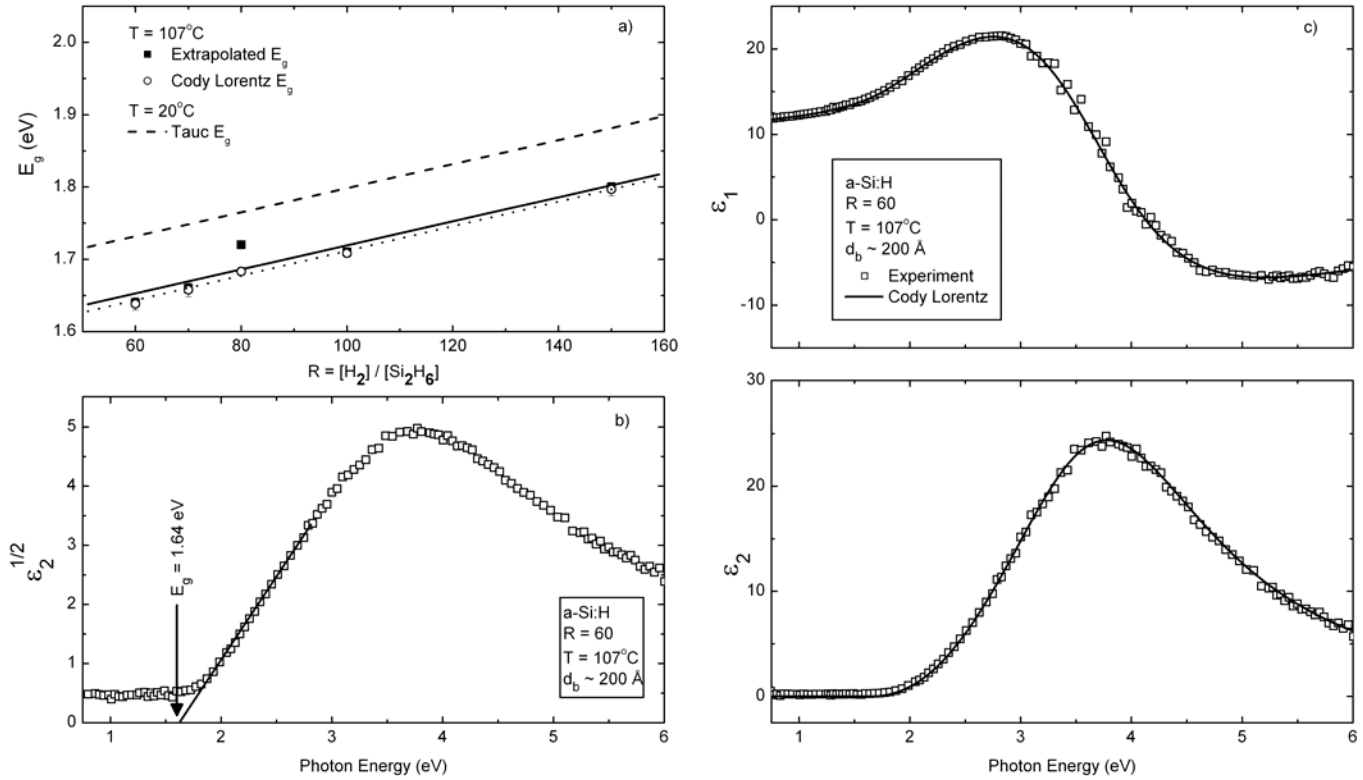

Fig. 3: **(**a) Optical band gap as a function of H_2-dilution flow ratio R determined from real time spectroscopic ellipsometry applying either a linear extrapolation of $\varepsilon_2^{1/2}$ spectra (solid points) or a complete fit using a Cody-gap-modified Lorentz oscillator function (open points), both relevant for the calibrated substrate temperature of 107°C (200°C nominal); the upper broken line is the result of a 0.08 eV adjustment that yields the room temperature Tauc gap; (b) a typical extrapolation that provides the gap given as the solid points in (a); (c) a Cody-gap-modified Lorentz oscillator fit to spectra in ε that provides the gap given as the open points in (a).

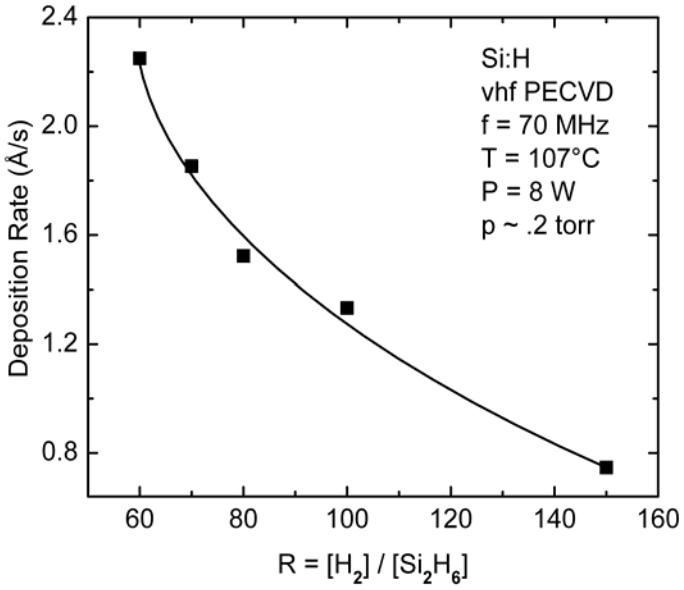

Fig. 4: Deposition rate as a function of hydrogen dilution for Si:H films prepared under vhf PECVD conditions that include: a calibrated substrate temperature of 107°C (200°C nominal), a total pressure of p = 0.2 Torr, and a vhf power of P = 8 W.

Turning to the structural evolution of the i-layer, Figure 4 shows first the deposition rate as a function of R. The rate decreases from ~ 2.3 to ~ 0.8 Å/s as R increases from 60 to 150. Figure 5 shows the surface roughness layer thickness versus bulk layer thickness during Si:H growth under two different H_2-dilution conditions, R. The key effects to be noted in this figure are the appearances of the amorphous-to-(mixed phase microcrystalline) roughening transition, denoted a $\rightarrow$ (a+μc), and the (mixed phase microcrystalline)-to-(single phase microcrystalline) transition, denoted (a+μc) $\rightarrow$ μc. The roughness evolution of these two films provide examples of depositions whereby the film remains amorphous throughout growth (R = 60) and whereby microcrystallites nucleate from the amorphous phase, grow, and eventually coalesce into a single-phase microcrystalline film (R = 150).

Similar roughness evolution data were acquired for additional depositions at varying R and used to compile the deposition phase diagram seen in Figure 6. This phase diagram demonstrates that under these deposition conditions films remain amorphous throughout ~2000 Å of bulk layer growth with R ≤ 80. At higher H_2 dilutions (80 < R ≤ 150), the Si:H films initially nucleate as a-Si:H on the substrate and develop a well-defined amorphous layer. As the bulk layer thickness increases, however, microcrystallites nucleate from the amorphous phase and cause the film to abruptly roughen due to the preferential growth of these microcrystallites [a $\rightarrow$ (a+μc)]. Ultimately, if the film reaches sufficient thickness, the microcrystallites begin to coalesce as noted by a peak and smoothening effect in the surface roughness profile [(a+μc) $\rightarrow$ μc] (see Fig. 5) such that a single-phase microcrystalline film grows soon thereafter.

The co-deposited films from this series deposited on the Ag/ZnO textured back-reflectors were then electronically characterized ex-situ to extract the open circuit voltage (V_{oc}), short circuit current (J_{sc}), fill factor (FF), and efficiency (η) as shown in Figure 7.

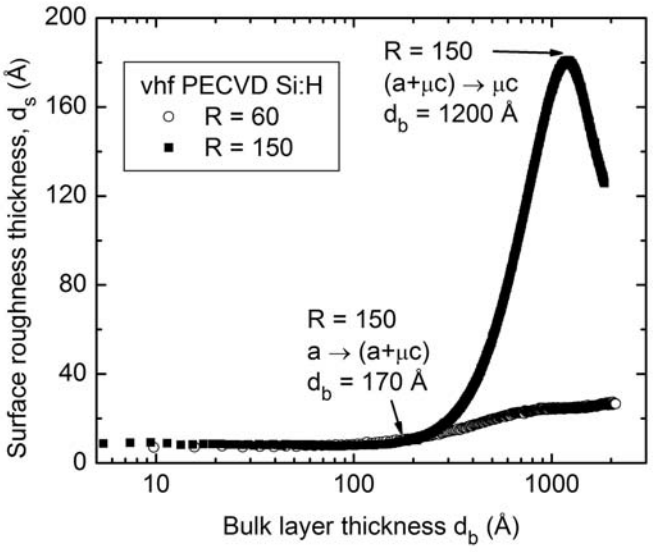

Fig. 5: Surface roughness evolution for a pair of Si:H films prepared under vhf PECVD conditions that include: a calibrated substrate temperature of 107 ^{o}C (200^{o}C nominal), a total pressure of p = 0.2 Torr, and a vhf power of P = 8 W. Examples of films in the fully amorphous growth regime (R = 60) and in the microcrystalline evolution regime (R = 150) are shown.

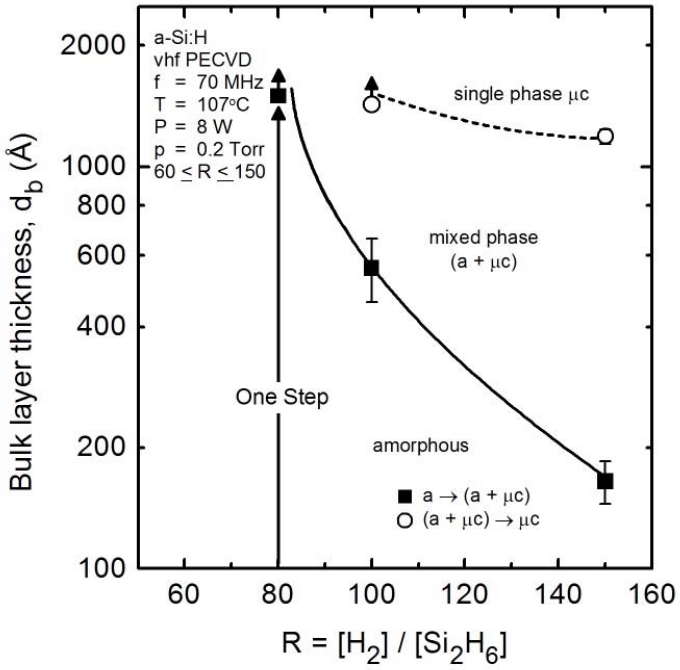

Fig. 6: A deposition phase diagram for Si:H films prepared under vhf PECVD conditions that include: a calibrated substrate temperature of 107 ^{o}C (200^{o}C nominal), a total pressure of p = 0.2 Torr, a vhf power of P = 8 W, and a variable H_2-dilution ratio of $60 \leq R \leq 150$. In this diagram, the thicknesses of the amorphous-to-(mixed-phase microcrystalline) transition (solid line, squares), and the (mixed-phase)-to-(single-phase) microcrystalline transition (dotted line, circles) are depicted. Up-arrows indicate that the transitions occur at thicknesses above the indicated values.

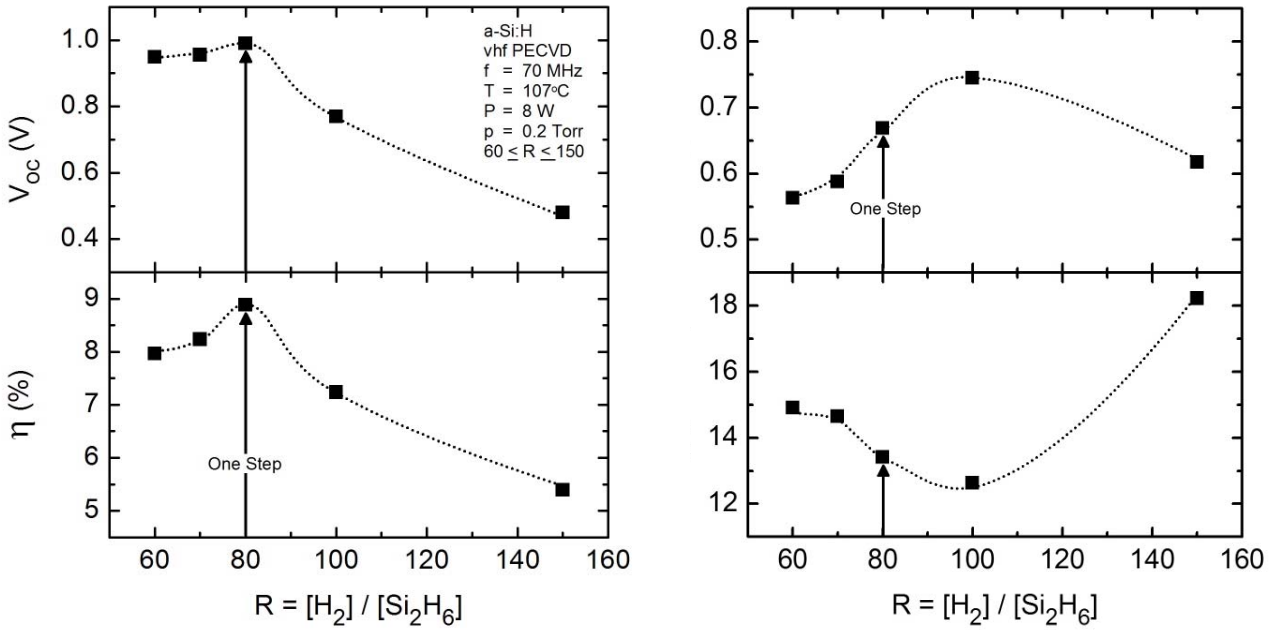

Fig. 7: Device characteristics for Si:H films prepared under vhf PECVD conditions that include: a calibrated substrate temperature of 107 °C (200°C nominal), a total pressure of p = 0.2 Torr, a vhf power of P = 8 W, and a variable H_2 dilution ratio of 60 ≤ R ≤ 150. These samples were deposited on a textured ECD back-reflector. The open circuit voltage (V_{oc}, upper left), efficiency (η, lower left), fill factor (FF, upper right), and short circuit current (J_{sc}, lower right) are plotted vs. R.

4. Discussion

The films shown in the phase diagram series of Fig. 6 have been designed with the intention of optimizing the top i-layer of a triple junction n-i-p device. Toward that end the films in this series have been deposited to bulk layer thicknesses of ~ 2000 Å with room temperature (T = 20°C) Tauc gaps ~ 1.8 eV. E_g increases as a function of R over the entire range studied. This increase typically accompanies an improvement in short range order in these films, as has been demonstrated previously for rf PECVD Si:H and its alloys [12, 14].

The deposition phase diagram of Fig. 6 provides insight into how these Si:H films evolve with thickness at different H_2 dilution levels and provides vital information for directing further optimization of solar cell performance. This diagram for PECVD from Si_2H_6 shows the standard features characteristic of previous diagrams from SiH_4. Specifically, increasing R causes (i) the onset of microcrystallite nucleation (i.e., the [a → (a+μc)] transition) to shift continuously to lower bulk layer thickness and (ii) the onset of coalescence of the preferentially growing microcrystallites (i.e., the [(a+μc) → μc] transition) to shift likewise. By understanding the nature of microcrystallite evolution and quantifying the volume fraction, it is possible to select the H_2 dilution in order to maximize film quality for one-step, multi-step, or graded layers. In the case of a one-step procedure, an optimum 1500 Å thick i-layer is to be expected at R = 80. This is the largest R value possible such that a 1500 Å thick film remains amorphous throughout its thickness during growth. At R=100, the a → (a+μc) transition occurs at 600 Å. In future work, a

finer grid in R will be used to better quantify the phase boundary; however, Fig. 6 suffices in order to correlate with device performance and suggest improvements.

It is noted immediately from the device performance characteristics in Figure 7 that the phase diagram prediction is verified, with R=80 providing the optimal 1500 Å thick, one-step i-layer in the device. For increasing R values above the optimum at R=80, the fall-off in open circuit voltage dominates and controls the peak in the efficiency of the solar cell. For R values lower than the optimum, the fall-off in fill factor (FF) dominates.

Considering first the variation in open-circuit voltage, V_{oc} is generally lower for R values below the optimum at R=80 due to the lower band gap; however, it is interesting that there is an abrupt increase in V_{oc} that defines the optimum with increasing R as the a $\rightarrow$ (a+μc) transition is approached. This is the protocrystalline regime, characterized by an improvement in ordering as well as an increase in band gap. Because V_{oc} is controlled by the film properties at the very top of the i-layer, there is an abrupt decrease in its value above R=80 due to the presence of crystalline nuclei at the top of the film. When the top of the film is mixed-phase, V_{oc} lies between the values for protocrystalline Si (~ 1 eV) and microcrystalline Si (~0.5 eV). For R values above the [(a+μc) $\rightarrow$ μc transition for a 1500 Å thick film, a V_{oc} appropriate for microcrystalline Si is expected.

The behavior of the fill factor (FF) with R suggests the possibility of an improvement in the cell performance with multistep processing. Figure 7 shows that although the FF increases with R, its maximum of 0.74 is reached at an R value larger than the maximum in V_{oc}. Because the FF is controlled predominantly by the bulk i-layer, the presence of crystallites near the top of the film -- that reduces the V_{oc} -- does not adversely affect the FF, which benefits from the improvement in bulk a-Si:H properties (i.e., increases in the band gap and protocrystalline ordering) with the increase in R from 80 to 100. It is expected that by depositing the bulk of the i-layer (~1000 Å) with R=100, then depositing a thin (~100 Å) low R substrate-memory-erasing layer -- similar to the starting n-layer -- before completing the cell with a second ~400 Å R=100 layer, one may be able to take advantage of an optimum V_{oc} and FF simultaneously. If this can be done successfully, the efficiency can be increased by ~0.5% from ~9% to 9.5%. The key, however, is to ensure that the substrate-memory-erasing layer first is successful, and second does not have a detrimental effect on the FF. The fact that the FF reaches 0.74 at R=100 even though the top half of the film is apparently mixed phase microcrystalline Si:H suggests that a thin low R layer will not be detrimental.

Finally turning to J_{sc}, the decrease between R=60 and 100 is easily understood in terms of a decrease in absorbance in the i-layer due to an increase in band gap at constant thickness. However, the significant increase in J_{sc} as the film enters the single phase microcrystalline region at R=150 must be attributed to the change in optical properties of the i-layer to predominantly microcrystalline in which case the film absorbs more than the corresponding thickness of top-cell amorphous i-layer material. Reduced top surface reflectance and enhanced light trapping, both due to the rough top surface of the cell, may also play a role.

5. Summary

In this study, a phase diagram in the plane of the bulk layer thickness d_b and the H_2-dilution ratio $R = [H_2]/[Si_2H_6]$ for Si:H deposited on the c-Si/(native-oxide)/n-layer structure exhibit features similar to those of the previous diagrams for Si:H growth from SiH_4 on R=0 a-Si:H. An $a \rightarrow (a+\mu c)$ transition is observed that shifts to decreasing d_b with increasing H_2-dilution ratio R, thus demonstrating a protocrystalline Si:H growth regime. Additionally, an $(a+\mu c) \rightarrow \mu c$ transition is observed under high H_2 dilution conditions. From this deposition phase diagram, an optimized ~1500 Å thick one-step i-layer is predicted for R = 80. This prediction is in good agreement with the device characteristics obtained from samples co-deposited on textured back-reflectors, as the R = 80 structure shows the maximum efficiency. This maximum is defined by a rapid increase in FF with R at lower R than the optimum and a rapid reduction in V_{oc} with R at higher R. The fact that V_{oc} and FF are optimized at different R values suggests a possible multi-step approach for efficiency improvement. The results of such efforts will be presented in the next quarterly report.

Acknowledgments

This research was supported by NREL (Subcontract Nos. NDJ-1-30630-01 and RXL-5-44205-06).

References

[1] J. Yang, A. Banerjee, and S. Guha, *Appl. Phys. Lett.* **70,** 2975 (1997).

[2] X. Deng, X.B. Liao, S.J. Han, H. Povolny, and P. Agarwal, *Solar Energy Mater. Solar Cells* **62**, 89 (2000).

[3] D.V. Tsu, B.S. Chao, S.R. Ovshinsky, S. Guha, and J. Yang, *Appl. Phys. Lett.* **71**, 1317 (1997).

[4] R.W. Collins and A.S. Ferlauto, *Curr. Opinion Solid State Mater. Sci.* **6**, 425 (2002).

[5] R.W. Collins, A.S. Ferlauto, G.M. Ferreira, C. Chen, J. Koh, R. Koval, Y. Lee, J.M. Pearce, and C.R. Wronski, *Solar Energy Mater. Solar Cells* **78**, 143 (2003).

[6] J. Koh, Y. Lee, H. Fujiwara, C.R. Wronski, and R.W. Collins, *Appl. Phys. Lett.* **73**, 1526 (1998).

[7] I. An, J.A. Zapien, C. Chen, A.S. Ferlauto, A.S. Lawrence, and R.W. Collins, *Thin Solid Films* **455**, 132 (2004).

[8] P. Lautenschlager, M. Garriga, L. Viña, and M. Cardona, *Phys. Rev. B* **36**, 4821 (1987).

[9] H. Arwin and D.E. Aspnes, *Thin Solid Films* **113**, 101 (1984).

[10] H. Fujiwara, J. Koh, P. I. Rovira, and R.W. Collins, *Phys. Rev. B* **61**, 10832 (2000).

[11] A.S. Ferlauto, G.M. Ferreira, J.M. Pearce, C.R. Wronski, R.W. Collins, G. Ganguly, and X. Deng, *J. Appl. Phys.* **92**, 2424 (2002).

[12] N.J. Podraza, C.R. Wronski, M.W. Horn, and R.W. Collins, *Mater. Res. Soc. Symp. Proc.* **910**, A10-01 (2006).

[13] R.M. Dawson, Y.M. Li, M. Gunes, D. Heller, S. Nag, R.W. Collins, C.R. Wronski, M. Bennett, and Y.-M. Li, *Mater. Res. Soc. Symp. Proc.* **258**, 595 (1992).

[14] R.W. Collins, J. Koh, A.S. Ferlauto, P.I. Rovira, Y. Lee, R.J. Koval, and C.R. Wronski, *Thin Solid Films* **364**, 197 (2000).

Section 3

Origin of optical losses in Ag/ZnO back-reflectors for thin film Si photovoltaics

D. Sainju, P.J. van den Oever*, N. J. Podraza , M. Syed #, J. Chen, J.A. Stoke, X. Yang, X. Deng, and R. W. Collins

Department of Physics and Astronomy, University of Toledo, Toledo, OH 43606, USA
* Dept. of Applied Physics, Eindhoven University of Technology, 5600 MB Eindhoven, The Netherlands
# Dept. of Physics & Optical Engineering, Rose-Hulman Institute of Technology, Terre Haute, IN 47803, USA

1. Introduction

A widely-used back-reflector (BR) for thin film Si solar cells in the substrate/BR/n-i-p configuration consists of opaque Ag followed by a ~3000 Å thick layer of ZnO, both sputtered onto a low-cost substrate such as stainless steel [1]. Quantum efficiency enhancement in the device arises due to reflection of near-infrared wavelengths back into the cell for possible absorption during additional passes. Furthermore, the Ag/ZnO interface is designed to be macroscopically rough so that the rays are obliquely scattered upon back-reflection to increase their optical path lengths. It is generally recognized that as macroscopic roughness of increasing thickness is incorporated, however, absorption losses at the Ag/ZnO interface are enhanced. Thus, the full potential of the BR concept has yet to be realized. For an improved understanding of these losses, we have analyzed the structural evolution of the Ag film as well as interface formation with ZnO by real time spectroscopic ellipsometry (SE). The study begins by preparing ultra-smooth Ag (surface roughness thickness: $d_s \sim 6$ Å) in order to assess the best-case scenario of Ag/ZnO interface formation. Then controlled increases in microscopic roughness on the Ag up to $d_s \sim 100$ Å are introduced by increasing the deposition temperature of the Ag. The goal is to evaluate changes in the interface optical losses even as the macroscopic roughness regime is entered. The observed changes in interface characteristics provide insights into the origin of the losses when the Ag/ZnO interface is macroscopically rough (i.e., "textured"). In fact, initial ex situ studies of back-reflectors with macroscopic roughness reported here support the validity of this approach.

2. Experimental Details

The Ag films were deposited by magnetron sputtering onto c-Si wafer substrates covered with native and thermal oxides ($d_{ox} \sim 15$-120 Å). Ultra-smooth Ag deposition is achievable under specific conditions using c-Si/SiO_2, which is itself atomically-smooth. The smoothest Ag film exhibits a microscopic roughness thickness $d_s = 6$ Å, as deduced by real time SE at the end of the deposition (typically corresponding to a bulk layer thickness of $d_b \sim 1500$ Å). These films are obtained at room temperatures using the lowest gas pressure possible (~ 4 mTorr), an argon gas flow of 10 sccm, and an intermediate target power (50 W). By elevating the substrate temperature to a nominal value of $\sim 190^{o}$C, a much larger microscopic roughness layer thickness of $d_s = 105$ Å is obtained by the end of the Ag deposition. ZnO is deposited at room temperature on the Ag surfaces having $6 \leq d_s \leq 105$ Å using the same sputtering conditions as for the Ag. Additional ZnO depositions were performed with different target powers, $25 \leq P \leq 100$ W, on Ag film surfaces with the same d_s. These results will be presented in a later report.

Ellipsometric measurements were performed using a rotating-compensator multichannel instrument that can provide spectra (0.75 to 6.5 eV) in (ψ, Δ) with a minimum acquisition time of 32 ms, as an average over a single pair of optical cycles. To improve precision, pairs of (ψ, Δ) spectra were collected within a time of ~ 1 s, as averages over ~ 30 optical cycle pairs. During the acquisition time for one set of (ψ, Δ) spectra, a bulk layer thickness of ~ 6 Å accumulates at the maximum deposition rate used here. Analyses of all spectra involve numerical inversion and least-squares regression algorithms. The angle of incidence was 64.88±0.09°.

3. Results and Discussion

By varying the nominal deposition temperature over the range $20 \leq T \leq 190^{o}C$, Ag films ~ 1500 Å thick with final microscopic surface roughness thicknesses, d_s, over the range $6 \leq d_s \leq 105$ Å were obtained; (see examples in Fig. 1). The ZnO films were deposited on these Ag films without a vacuum break. The evolution of each ZnO film was modeled using a layer with the optical properties of bulk ZnO and a Ag/ZnO interface layer with optical properties showing features that are observed neither in Ag nor in ZnO. Inclusion of such an interface layer has been shown to significantly improve the fit to the full real time spectroscopic data set [2]. Figure 2 shows the Ag/ZnO interface layer thickness d_i as a function of initial Ag surface roughness thickness d_s. During ZnO growth, the interface layer thickness increases approximately linearly with time until it reaches a stable saturation thickness, as has been shown previously [2]. The interface thickness shown in Fig. 2 is obtained by averaging all d_i from the saturation point until the end of the deposition. This average interface thickness is found to correlate with the starting microscopic roughness on the Ag with extrema values of d_i = (40, 233) Å for d_s = (6, 105) Å.

The interface optical properties are extracted by numerical inversion in the same analysis procedure that provides the ZnO bulk and Ag/ZnO interface layer thicknesses. Figure 3 shows the real and imaginary parts of the dielectric function of the interface layer for a sample with initial Ag surface roughness thickness of 100 Å. The inverted dielectric functions (circles) were fit using a Kramers-Kronig consistent model (lines). The features in the data and model exhibit

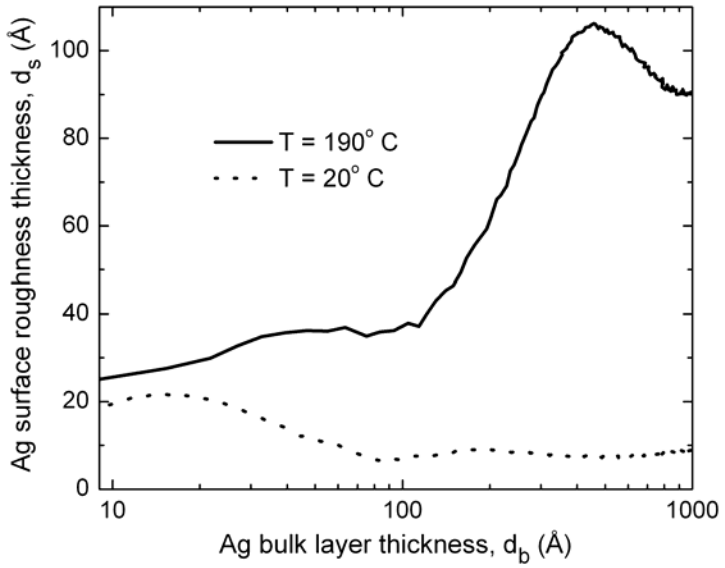

Fig. 1: Evolution of microscopic surface roughness layer thickness with bulk layer thickness for Ag films sputtered onto oxidized Si at two nominal temperatures, T = 20 and 190°C. Microscopic roughness thickness is determined assuming a surface layer with optical properties determined by an effective medium theory as a mixture of bulk material and void.

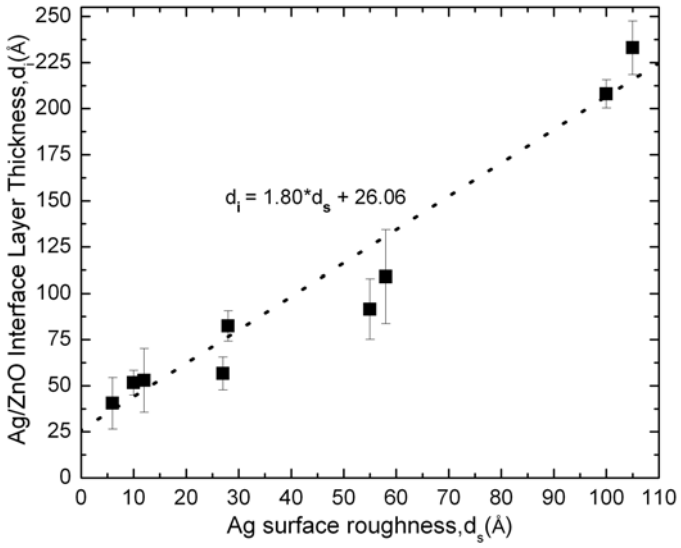

Fig. 2: Ag/ZnO interface layer thickness (d_i) obtained as an average versus time during ZnO deposition (after the saturation thickness in d_i has been reached) plotted as a function of initial Ag surface roughness thickness (d_s).

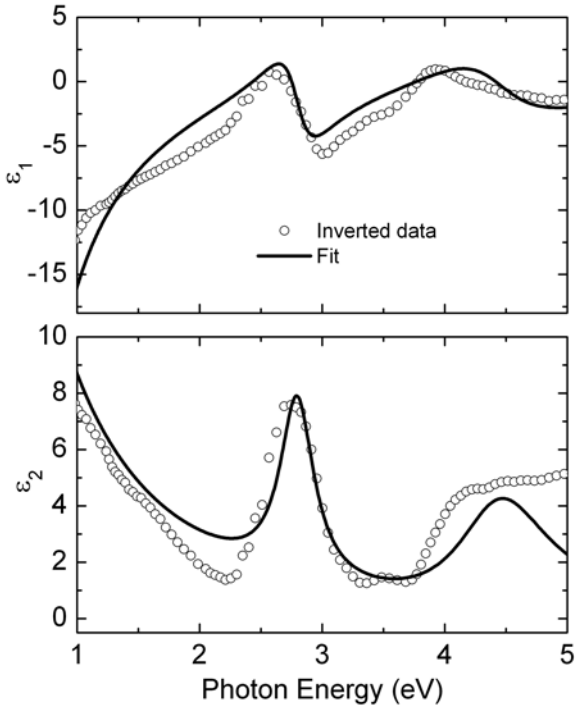

Fig. 3: Real (upper) and imaginary (lower) parts of the dielectric function of the Ag/ZnO interface layer for the sample with initial Ag surface roughness of d_s = 100 Å, obtained by exact inversion of (ψ, Δ) spectra (circles); a fit using a Kramers-Kronig consistent model is also shown (lines).

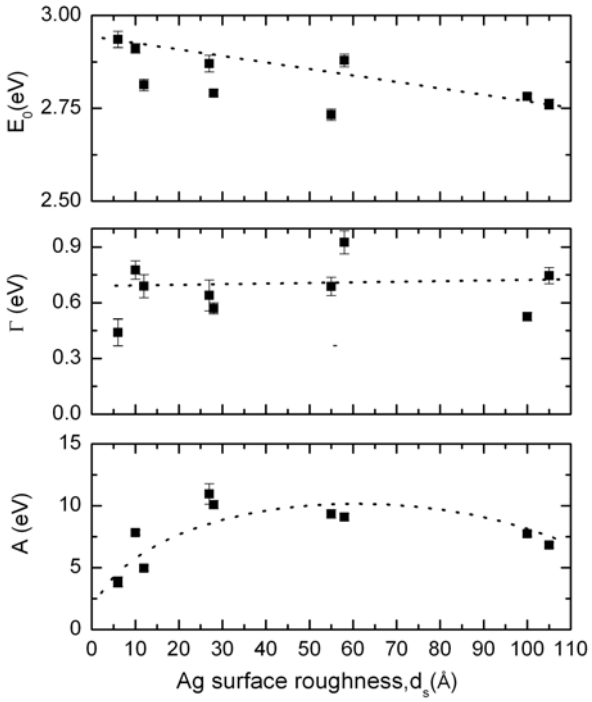

Fig. 4: Resonance energy (E_0), broadening (Γ), and amplitude (A) of the plasmon band associated with the Ag/ZnO interface layer plotted as functions of initial Ag surface roughness thickness, d_s. To obtain this information, the plasmon band has been modeled as a single Lorentz oscillator.

similar characteristics which support the validity of the real time SE data analysis. The interface layer analysis includes (i) a free electron component modeled using the Drude expression, (ii) a plasmon band modeled as a Lorentz oscillator, and (iii) a bound electron absorption feature modeled assuming transitions between parabolic bands near a band structure critical point [3].

The Lorentz oscillator parameters of the plasmon band (ii), which has also been suggested in earlier studies of the Ag/ZnO interface [4], are plotted versus Ag d_s in Fig. 4. The top panel shows that the energy of the plasmon band decreases as the Ag d_s value increases. For the range of d_s investigated here, this shift is ~200 meV. For a plasmon propagating at the surface of a metal with ambient dielectric function ε_a, the plasmon peak is predicted to occur at a photon energy of $E_0 \sim E_p(1+\varepsilon_a)^{-1/2}$. The values $E_p = 8.8$ eV for the bulk free-electron plasmon energy of Ag and $\varepsilon_a = 4.0$ for ZnO at the observed E_0 of 2.85 eV together yield $E_0 = 3.9$ eV for Ag/ZnO. The significantly lower value in Fig. 3 can be attributed to protrusions on the Ag surface that lead to localized plasmon-polariton modes. For simple spherical protrusions, these modes appear at: $E_0 \sim E_p\{1 + [(2+Q)/(1-Q)]\varepsilon_a\}^{-1/2}$, where Q is the volume fraction of metal protrusions in the surface layer [3]. Taking $E_p = 8.8$ eV and $\varepsilon_a = 4.0$, then this expression gives $E_0 = 2.93$ eV in the limit of Q=0 and $E_0 = 2.74$ eV when Q=0.1. Thus, electronic resonances within surface protrusions can account for the plasmon energy of Fig. 4, and the increase in the volume fraction associated with the protrusions with Ag d_s can account for the red-shift. The center panel in Fig. 4 shows the width of the plasmon band versus Ag d_s. A value of $\Gamma = 0.7 \pm 0.25$ eV characterizes results for all samples. A strong broadening effect (consequently short scattering time) relative to that of bulk Ag (~ 0.02 eV), can be attributed to surface scattering due to the small size of the structures; disorder of the Ag may also play a role. Finally, the bottom panel of Fig. 4 suggests that the amplitude of the plasmon band increases with increasing Ag roughness thickness.

A further increase in the initial surface roughness of Ag into the macroscopic range (as in the highest efficiency solar cell structures) may cause a red shift of the plasmon band into a region where it will impact solar cell quantum efficiency. For example when Q is 0.5, E_0 is 1.9 eV which, when coupled with a plasmon band full-width-at-half-maximum of 0.7 eV, is expected to yield significant absorption within the critical region for back reflector operation. As a first step toward assessing this possibility, Fig. 5 depicts the interface layer dielectric functions for two samples with different initial Ag surface roughness thicknesses, 28 and 105 Å. Samples with higher Ag surface roughness exhibit increased low energy absorption losses, as can be seen from the ε_2 spectra. Also depicted in Fig. 5 are the results of an ex situ study in which ε_1 and ε_2 for the Ag/ZnO interface have been extracted for a fully textured back reflector structure fabricated by Energy Conversion Devices, Inc. (ECD). Presumably it is the increased scale of the surface roughness (caused by texturing) for the ECD back reflector structure that yields Ag/ZnO dielectric functions characteristic of low energy plasmon resonance behavior as indicated by its ε_2 spectrum. In fact, the associated reflectance prediction indicates a significant reduction in reflectance over the near-infrared spectral range where high back-reflector performance is desired for enhanced light collection in the solar cell.

Ex situ reflectance measurements have also been performed on the Ag/ZnO structures at normal incidence in order to evaluate the optical models developed by real time SE. It is important to note that the observed reflectance spectra cannot be modeled successfully without including an interface layer of approximately the same thickness as deduced by real time SE.

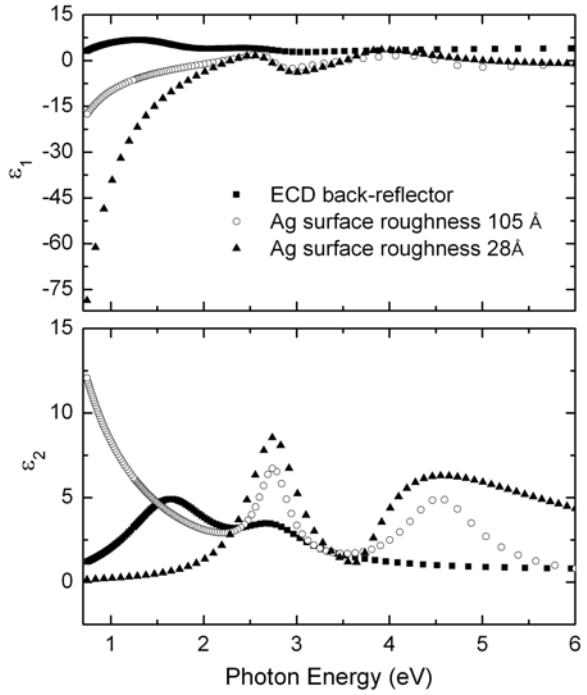

Fig. 5: (left) Real and imaginary parts of the fitted dielectric functions of the interface layer for two Ag/ZnO samples prepared at University of Toledo with two different initial Ag surface microscopic roughness layer thicknesses; also shown are corresponding results for a Ag/ZnO back-reflector prepared at Energy Conversion Devices, Inc. with the inclusion of macroscopic roughness (or texture).

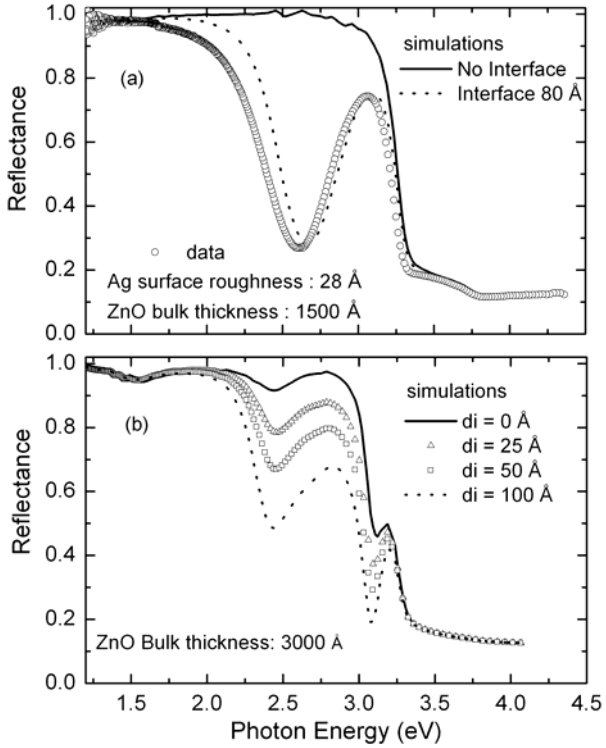

Fig. 6: (a) Reflectance data and simulations for a ZnO thickness of d_b = 1500 Å and interface layer thicknesses of d_i = 0 and 80 Å; (b) reflectance simulations with d_b = 3000 Å and different d_i values from 0 to 100 Å, whereby the interface ε is determined from the data for d_s = 28 Å.

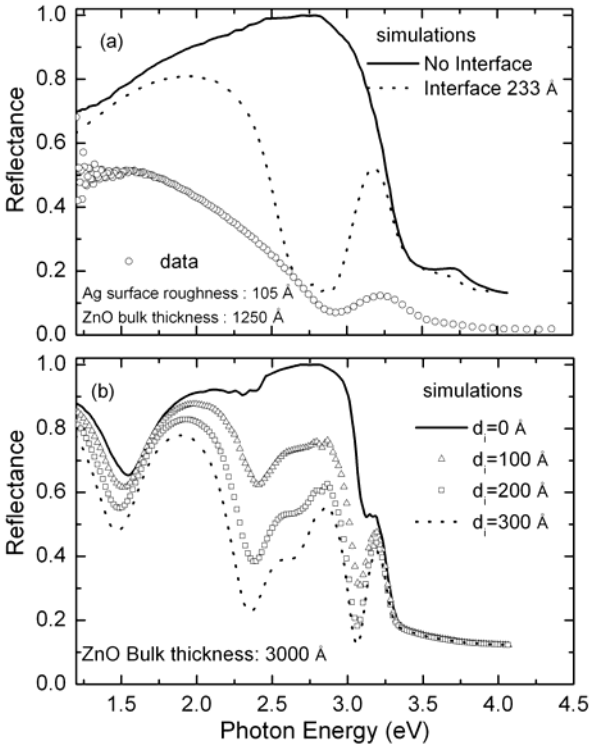

Fig. 7: (a) Reflectance data and simulations for a ZnO thickness of d_b = 1250 Å and interface layer thicknesses of d_i = 0 and 233 Å; (b) reflectance simulations with d_b = 3000 Å and different d_i values from 0 to 300 Å, whereby the interface ε is determined from the data for d_s = 105 Å.

Figure 6(a) shows the measured reflectance for the Ag/ZnO structure prepared on Ag with d_s = 28 Å (open circles). In fact, the reflectance is consistent with an optical model (dotted line) that includes the same 80 Å interface layer as deduced in the real time SE analysis. Resonant enhancement of losses due to this interface layer occurs for photon energies within a broad band centered at 2.6 eV. The strong minimum at 2.6 eV occurs when an interference minimum in R overlaps the plasmon energy which leads to a strong coupling of the energy from the optical field into the plasmon modes. In spite of this effect in the visible part of the spectrum, no significant losses are observed in the near-infrared below 1.6 eV. Thus, this interference enhanced plasmon absorption is of marginal importance as a loss mechanism in solar cells – at least for this particular sample structure. Figure 6(b) shows reflectance simulations for a thicker ZnO layer (d_b = 3000 Å), demonstrating that the dominant losses in the spectral range of interest for solar cell back-reflectors (1.2 to 1.5 eV) are independent of d_i for this particular type of Ag/ZnO interface (i.e., for the observed d_i range and associated dielectric function). In this situation, the residual losses are due to intrinsic absorption in the Ag, again enhanced by interference.

Figure 7 demonstrates that a different interface type, resulting from a higher initial Ag surface roughness thickness strongly affects the reflectance spectrum. In this situation, Fig. 7(a) shows the measured reflectance for a Ag/ZnO structure prepared on Ag with d_s = 105 Å (open circles) as well as the simulated reflectance assuming a specular structure with a 233 Å interface, which is the value deduced in the real time SE analysis (applying the interface dielectric function deduced in the same analysis). The large differences between the measured and simulated reflectance spectra in this situation can be attributed to the increased level of light scattering for the thicker initial Ag surface roughness, entering the macroscopic roughness regime. Figure 7(b) represents a series of simulations of different ZnO/Ag structures whereby the ZnO bulk layer thickness is fixed at 3000 Å, while the interface layer thickness is varied within the range $0 \leq d_i \leq 300$ Å. With the dielectric function for this interface, significant optical losses occur in the region of 1.2-1.5 eV. More importantly, the reflectance losses increase steadily in this region with increasing interface layer thicknesses.

4. Summary

Real time SE has been applied to investigate the optical properties of Ag/ZnO interfaces in back-reflectors in the configuration used for n-i-p thin film Si solar cells. In particular, the effects of starting Ag surface roughness ($d_s \sim 6 - 105$ Å) on the nature of this interface have been explored. Even for the smoothest starting Ag surfaces (6 Å surface roughness thickness), a plasmon absorption band is detected in the optical properties of the observed ~ 40 Å thick interface layer. The characteristics of this band show a correlation with the starting Ag roughness layer, including a red shift in the plasmon peak energy with increasing d_s. We have corroborated the findings of real time SE using ex situ reflectance measurements, finding significant absorption losses in the visible range due to interference-enhanced plasmon absorption. For the specular Ag/ZnO studied here, these losses do not extend sufficiently far into the infrared to affect cell performance for ZnO deposited on relatively smooth Ag surfaces. When the underlying Ag surface roughness is thick enough ($d_s \sim 100$ Å) to significantly influence the nature of the interface dielectric function, optical losses due to the interface layer thickness and interference-enhanced plasmon absorption red-shift into the 1.2-1.5 eV range, where they are expected to strongly impact back-reflector performance in solar cells. Future efforts will be

devoted to real time SE studies of Ag/ZnO further into the macroscopic roughness regime and to methods for mitigating the absorption losses in this regime.

Acknowledgements

This research is supported by NREL TFPPP Subcontract No. ZXL-5-44205-06.

References

[1] X. Deng and E.A. Schiff, in: *Handbook of Photovoltaic Science and Engineering*, edited by A. Luque and S. Hegedus (Wiley, New York, 2003), p. 505.

[2] D. Sainju, P.J. van den Oever, N.J. Podraza, M. Syed, J.A. Stoke, J. Chen, X. Yang, X. Deng, and R.W. Collins, *Proceedings* of the *4th World Conference on Photovoltaic Energy Conversion*, (IEEE, Piscataway, NJ, 2006), p. 1732.

[3] R.W. Collins and A.S. Ferlauto, in *Handbook of Ellipsometry*, (William Andrew, Norwich, NY, 2005), p. 93.

[4] J. Springer, A. Poruba, L. Mullerova, M. Vanecek, O. Kluth, and B. Rech, *J. Appl. Phys.* **95**, 1427.